CHAPTER 4

RESULTS AND DISCUSSION

This chapter is presented of the all results and discussion of the characteristic thermoelectric materials, thermoelectric properties, power generation of themogenerator and application as follows:

SYNTHESIS $Ca_{1-x}Bi_xMnO_3$ AND $Ca_3Co_4O_9$ + Ag 10 wt% POWDER THERMOELECTRIC MATRERIALS

Synthesis powder of $Ca_{1-x}Bi_xMnO_3$

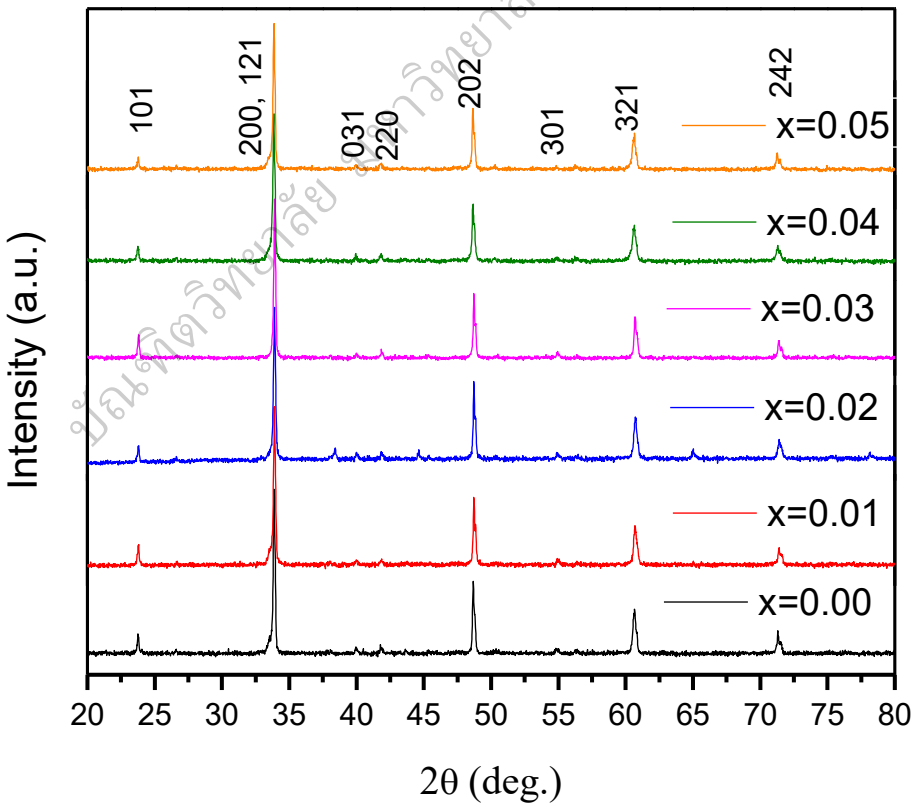

Figure 35 XRD patterns of $Ca_{1-x}Bi_xMnO_3$ powders for (x = 0.00, 0.01, 0.02, 0.03, 0.04, 0.05) samples at room temperature

The X-ray diffraction patterns of sintered $Ca_{1-x}Bi_xMnO_3$ (x = 0, 0.01, 0.02, 0.03, 0.04 and 0.05) powders at room temperature, are shown in Figure 35. The diffraction pattern of all powders were showed single phase correspond with $CaMnO_3$ (CMO) un-doped sample phase indicating an orthorhombic perovskite structure in *Pnma* space group (PDF Card – 00-050-1746). The lattice parameter was calculated from XRD data meanwhile, the cell volume and theoretical density of all sample as shown in Table 3. The result of lattice parameter and cell volume were linearly increased with increasing Bi doping contents (Kabir,et al., 2015). This behaviour was affected from substitution of Bi on Ca-site which similar ionic radius of the element ccording to these reported in the $Ca_{1-x}Bi_xMnO_3$ system, Bi sever as electron doping. Then the electron doping was induced the present by Mn^{3+} within Mn^{4+} matrix of CMO and the difference ionic radius between Mn^{3+} (0.64 Å) was larger than Mn^{4+} (0.53 Å) which distort the octahedral in CMO structure. So that, it was found that lattice the parameter increased with increasing Bi content (Kabir,et al., 2015; Huang, et al., 2008; Bhaskar, et al.,2013).

Table 3 Lattice parameters, densities of $Ca_{1-x}Bi_xMnO_3$ (x = 0, 0.01, 0.02, 0.03, 0.04 and 0.05) samples

Sample Bi content (x)	a (Å)	b(Å)	c(Å)	Unit cell Volume ($Å^3$)	Theoretical density (g/cm^3)	Experimental density (g/cm^3)	Relative density (%)
0	5.2895	7.4949	5.2257	207.172	4.58	4.25	92.79
0.01	5.2989	7.4679	5.2399	207.338	4.63	4.21	90.92
0.02	5.2801	7.4683	5.2802	208.214	4.67	4.31	92.92
0.03	5.3271	7.4890	5.2466	208.215	4.72	4.34	91.94
0.04	5.2906	7.4685	5.2697	209.312	4.75	4.42	93.05
0.05	5.3161	7.4687	5.2742	209.412	4.80	4.47	93.15

The experimental density of samples was increased with increasing of doping Bi contents as shown in Table 3. The density increased because Bi was heavier mass contribution of CMO and another factor used hot pressing method for prepared all sample helpful decreasing porosity on the samples. The theoretical density of all sample was calculated from lattice constant of XRD data and the relative density show good compactness.

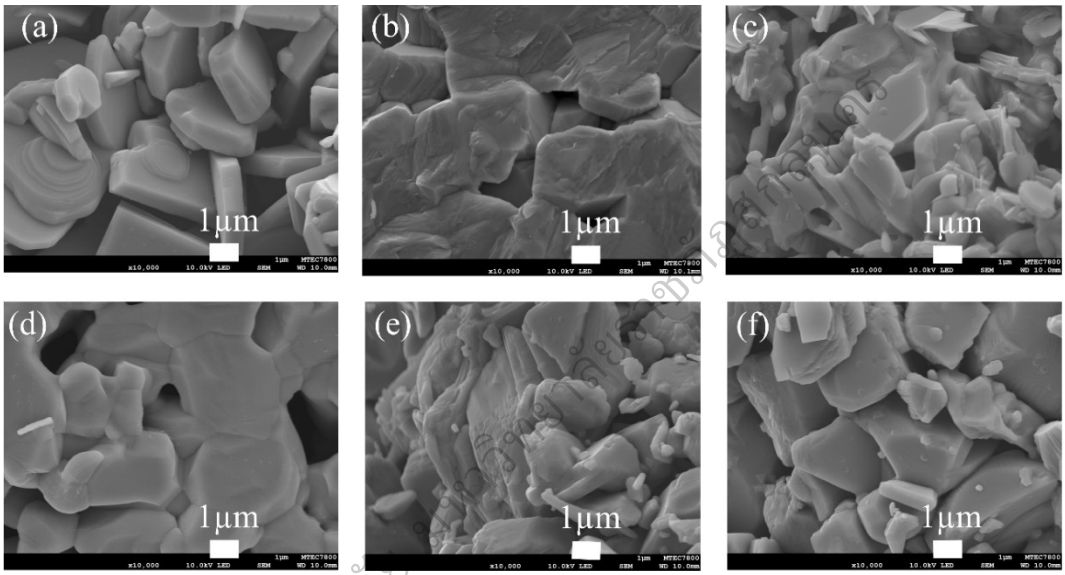

Figure 36 SEM images of bulk $Ca_{1-x}Bi_xMnO_3$ (a) x = 0.00, (b) x = 0.01, (c) x = 0.02, (d) x = 0.03, (e) x = 0.04 and (f) x = 0.05 samples

The microstructure of bulk $Ca_{1-x}Bi_xMnO_3$ (a) x = 0.00, (b) x = 0.01, (c) x = 0.02, (d) x = 0.03, (e) x = 0.04 and (f) x = 0.05 samples, are shown in Fig. 36. The morphology of all sample were showed good compactness, and decreased grain connecting of pore and micro-cracking in the sample due to the density increased by using HP method when compare with report (Kabir,et al., 2015).

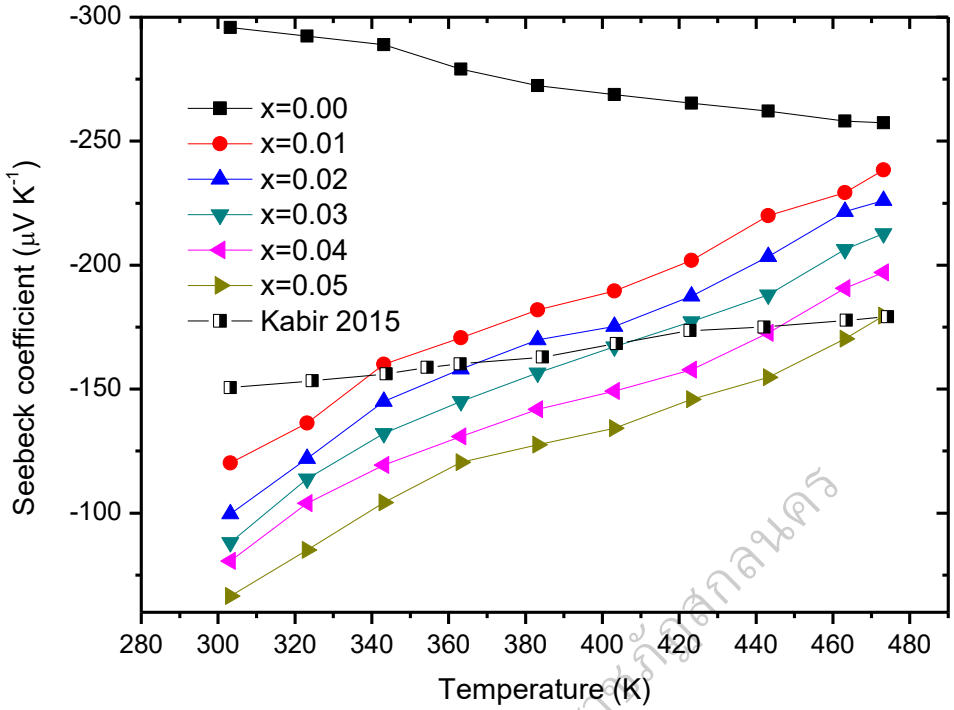

Figure 37 The temperature dependent Seebeck coefficient of $Ca_{1-x}Bi_xMnO_3$ samples

The Seebeck coefficient of $Ca_{1-x}Bi_xMnO_3$ (x = 0, 0.01, 0.02, 0.03, 0.04 and 0.05) samples were measured by steady state technique at 300 K to 473 K in atmosphere, are shown in Fig. 37. The S of all sample showed negative value indicate that an n–type electrical conduction behavior and un–doped CMO sample showed large absolute value of S and typical semiconductor behavior. On the other hand, all doped samples showed metallic conduction behavior and the S decreased with increase Bi contents. From this behavior was attributed the increasing carrier concentration of CMO which observed lattice parameter increased in Table 3, which accord with reported before (Kabir,et al., 2015; Huang, et al., 2008; Bhaskar, et al.,2013). In addition, the grain connection have been effected in S because increasing of carrier mobility. Thus, the S all samples were evaluated from this equation.

$$S = \frac{\pi^2 k_B^2 T}{eE_F} \qquad (4.1)$$

Where π, k_B, T, e and E_F were π, Boltzmann constant, absolute temperature, electron

charge and Fermi level, respectively. The S is inversely proportional to Fermi level. The Seebeck coefficient can evaluated by Fermi level from S at 303 K, which were 0.075 eV, 0.184 eV, 0.222 eV, 0.251 eV, 0.275 eV and 0.333 eV for x = 0, 0.01, 0.02, 0.03, 0.04 and 0.05, respectively. These result mean the Bi doping were increased Fermi level of $CaMnO_3$ un-doped. When Ca^{2+} substituted Bi^{3+} which the Bi^{3+} was a donor ions. Then the increasing of carrier concentration has a directly result to shift of occupied energy level structure to higher binding energy. Therefore, this phenomenal Fermi level increasing was attributed to the increase of Bi doping content (Zhu, et al., 2015). The S of doped sample were decreased from un-doped 7.38 %, 12.21 %, 17.35 %, 23.47 % and 30.24 % follow by x=0.01 to 0.05 at 473 K, respectively.

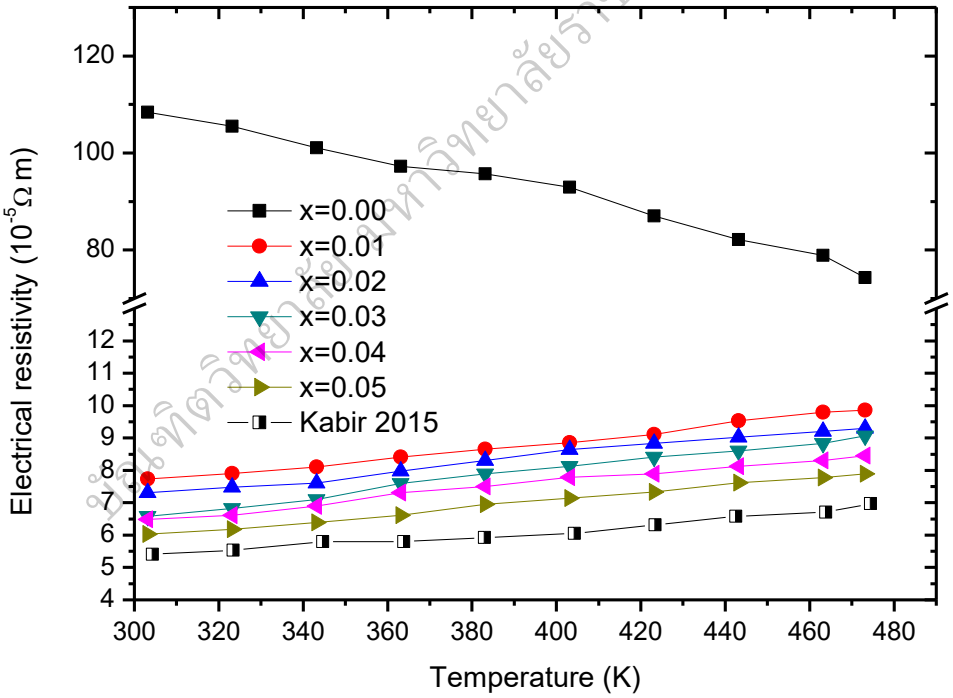

Figure 38 The temperature dependent electrical resistivity of $Ca_{1-x}Bi_xMnO_3$ samples

The electrical resistivity of $Ca_{1-x}Bi_xMnO_3$ (x = 0, 0.01, 0.02, 0.03, 0.04 and 0.05) samples, seem in Figure 38. The ρ of un-doped CMO was deceased with increasing temperature indicate of semiconductor behavior. However, all doped samples showed ρ was increased with increasing temperature indicate metallic behavior and also the ρ decreased with increasing doped Bi contents. Because the effect from Bi serving increased carrier concentration according with previous work (Zhu, et al., 2015; Bhaskar, et at., 2013). In addition, the carrier mobility were increased from grain connection helpful for ρ decreasing. The ρ of doped sample were decreased from un-doped 86.72 %, 87.48 %, 87.79 %, 88.61 % and 89.37 % follow by x=0.01 to 0.05 at 473 K, respectively.

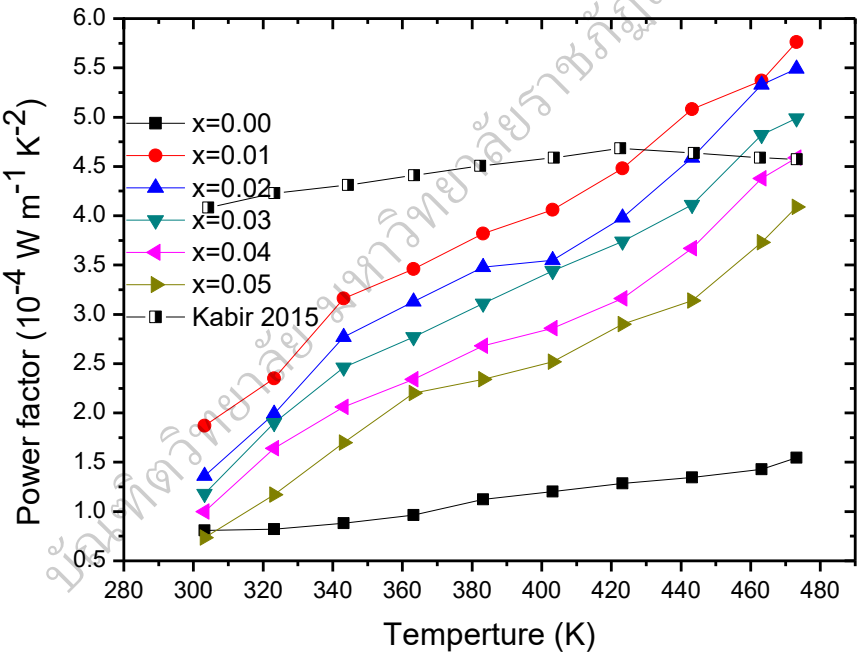

Figure 39 The temperature dependent of power factor for $Ca_{1-x}Bi_xMnO_3$ samples

The power factor of all samples were evaluated by S and ρ values as equation $\frac{S^2}{\rho}$. The un-doped sample was showed lowest PF due to high S but in ρ is very high when compared with doped sample. The maximum of PF shows in condition $Ca_{0.99}Bi_{0.01}MnO_3$ about 5.7 $\times 10^{-4}$ W m^{-1} K^{-2} and the trend of all doped sample increased with increasing temperature.

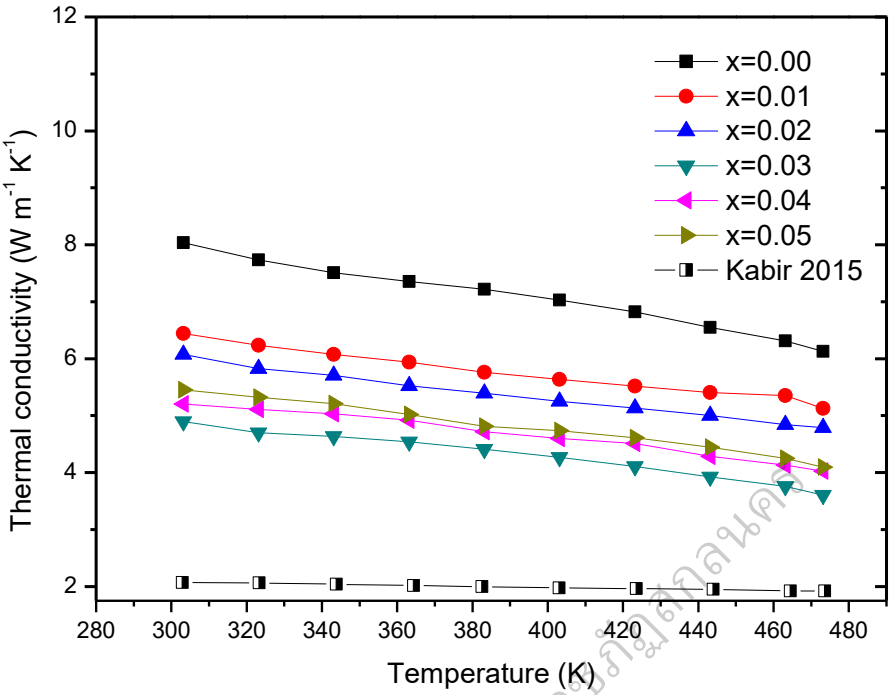

Figure 40 The temperature dependent total thermal conductivity for all sample at temperature range of 300 to 473K

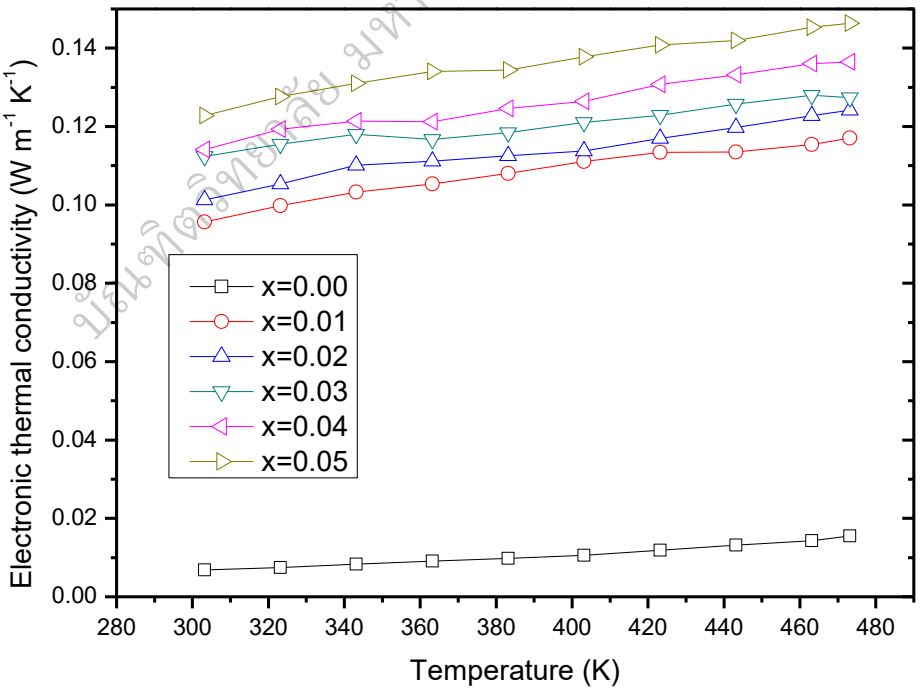

Figure 41 The temperature dependent of electronic thermal conductivity for all sample at temperature range of 300 to 473K

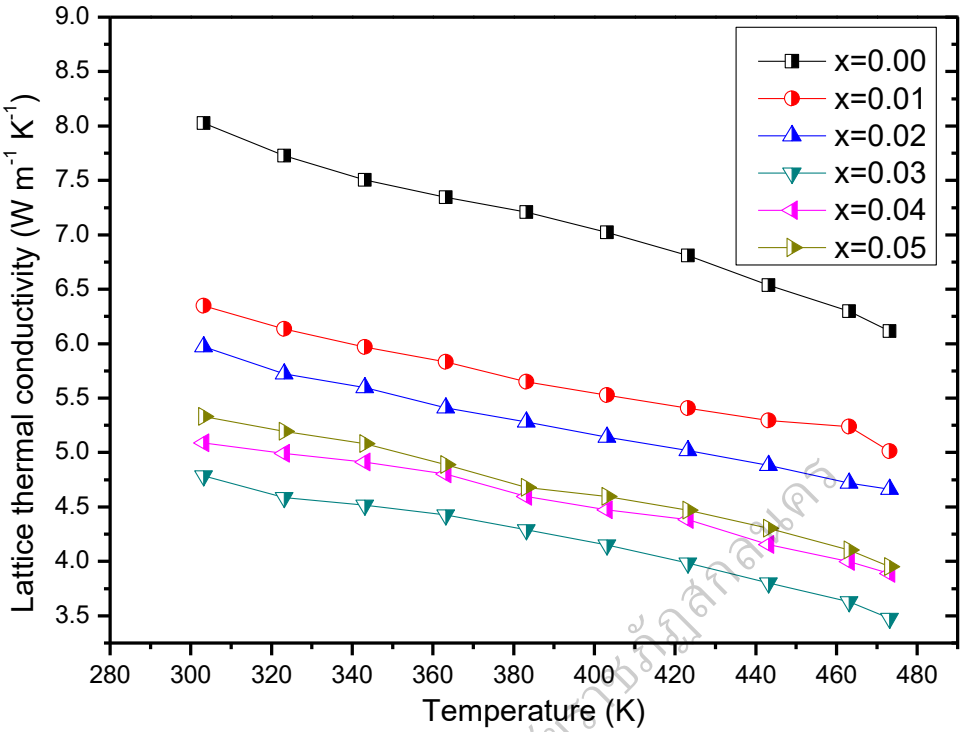

Figure 42 The temperature dependent of lattice thermal conductivity for all sample at temperature range of 300 to 473K

The total thermal conductivity (close symbols), electronic thermal conductivity (open symbols) and lattice thermal conductivity (half close symbol) for all sample at temperature range of 300 to 473K as shown in Fig. 40, 41 and 42, respectively . The total thermal conductivity (κ) was evaluated by combination lattice thermal conductivity (κ_l) and electronic thermal conductivity (κ_e) follow this equation $\kappa = \kappa_l + \kappa_e$. The electronic thermal conductivity was calculated from Wiedemann–Franz's law equation by using electrical resistivity.

$$\kappa_e = \frac{LT}{\rho} \qquad (4.2)$$

where κ_e , L , T and ρ are electronic thermal conductivity, Lorentz constant, absolute temperature and electrical resistivity, respectively. The lattice thermal conductivity (κ_l) were evaluated by $\kappa_l = \kappa - \kappa_e$. The κ_e of all samples doped were increased with increasing temperature as well as of doped Bi contents

(Kabir, et al.,2015). Then compared between κ, it was clearly the major of value got from the κ_l. Therefore, the κ with un-doped CMO was compared with all doped samples show lower than un-doped sample indicating that Bi substitution at Ca-site can be decreased of κ. The κ of x= 0.01, 0.02 and 0.03 samples were decreased by reduction of κ_l.The possible about this behavior was that both the crystal distortion and oxygen vacancy contributed to decrease of κ. The strong crystal distortion was created enhance phonon scattering resulting in the decreased of κ. However, the doped sample x>0.03 was increased slightly due to crystal distortion and increased oxygen vacancy shows in the relative density value and main factor for phonon scattering more Bi substitution which increase κ (Zhu, et al.,2015; Kabir, et al.,2015). The κ of doped samples were decreased from un-doped 16.31 %, 21.90 %, 41.22 %, 34.36 % and 33.16 % follow by x=0.01 to 0.05 at 473 K, respectively.

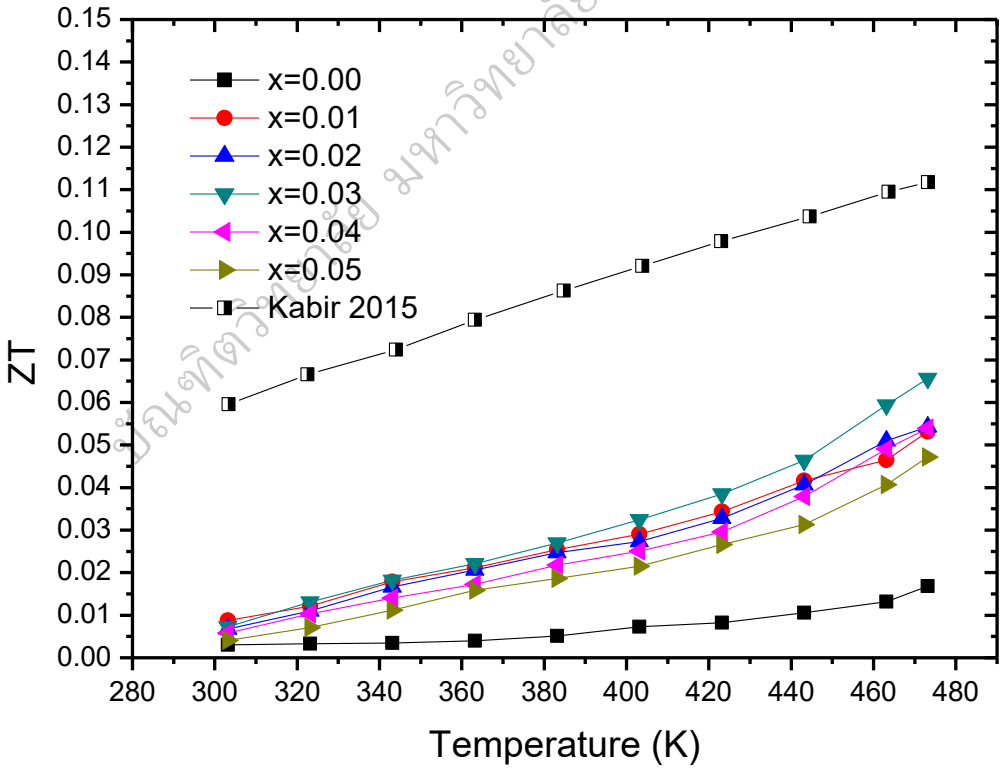

Figure 43 The relationship between temperature dependent ZT for $Ca_{1-x}Bi_xMnO_3$ samples

The dimensionless figure of merit of all samples, are shown in Figure 43. Normally, all doped samples show higher ZT value more than the un-doped CMO. The $Ca_{0.97}Bi_{0.03}MnO_3$ shows highest ZT value about 0.065 at 473 K together with un-doped sample mean 3 time at same temperature. Because in this condition lowest κ was 3.60 W m^{-1} K^{-1} and optimized PF.

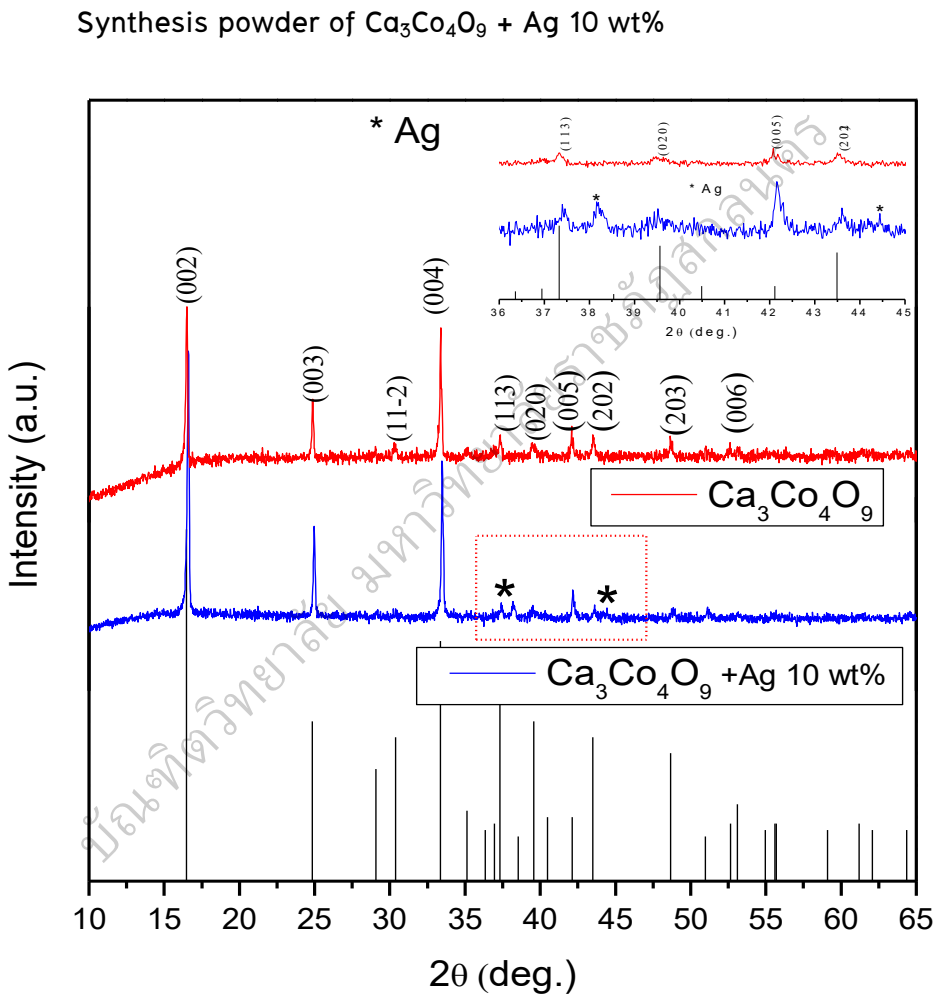

Figure 44 XRD patterns of sintered bulk $Ca_3Co_4O_9$ + Ag 10 wt% and $Ca_3Co_4O_9$

XRD measurement was performed on the sintered powder of SSR method samples as shown in Figure 44. The XRD patterns of the samples agree with the $Ca_3Co_4O_9$ (CCO) and monoclinic structure, except for weak diffraction peaks from

the secondary phase of Ag (marked *) in the $Ca_3Co_4O_9$ + Ag 10 wt% (CCO + Ag). No impurity phase diffraction peak from compound such as $CaCO_3$ or Co_3O_4 were observed. Lattice parameters of CCO and CCO + Ag were a=4.4734 Å, b_1=4.3722 Å, c=10.1536 Å and a=4.4734 Å, b_1=4.3779 Å, c=10.155 Å, respectively. The density of CCO and CCO + Ag samples were 4.066 g/cm^3, 4.109 g/cm^3 and relative density 86.85 %, 87.86 %, respectively. A strong peaks (00l) in each XRD pattern indicated for the grain-orientation of CCO+Ag. Moreover, the orientation degree can be determine by Lotgering factor follow; (Lotgering, 1959, pp. 113-123)

$$f = \frac{(P - P_0)}{(1 - P_0)} \tag{4.3}$$

where

$$P = \frac{\sum I(00l)}{\sum I(hkl)} \tag{4.4}$$

The P is the grain oriented sample and P_0 is randomly-oriented powders. In this study, P_0 is calculated from the XRD data of the standard card. The c-axes of crystal grains are completely aligned along the pressing direction. The calculated orientation degrees of CCO+Ag sintered samples are about 0.4. These observations suggest that the alignment of plate-like CCO grains is enhanced during the densification process. Moreover, the orientation degree is also improved by adding small amounts of Ag particles the grain-boundary sliding associated with deformation in the radial direction has been applied to explain grain alignment in samples consisting of plate-like grains under pressure sintering. The CCO+Ag was showed anisotropic materials corresponds well to Ning et al. work on the measurement thermoelectric properties in a different direction (parallel and perpendicular to pressure axis) which perpendicular exhibited the better higher thermoelectric performance (Wu, et al.,2014). So the cutting materials for fabrication was should considering in perpendicular direction.

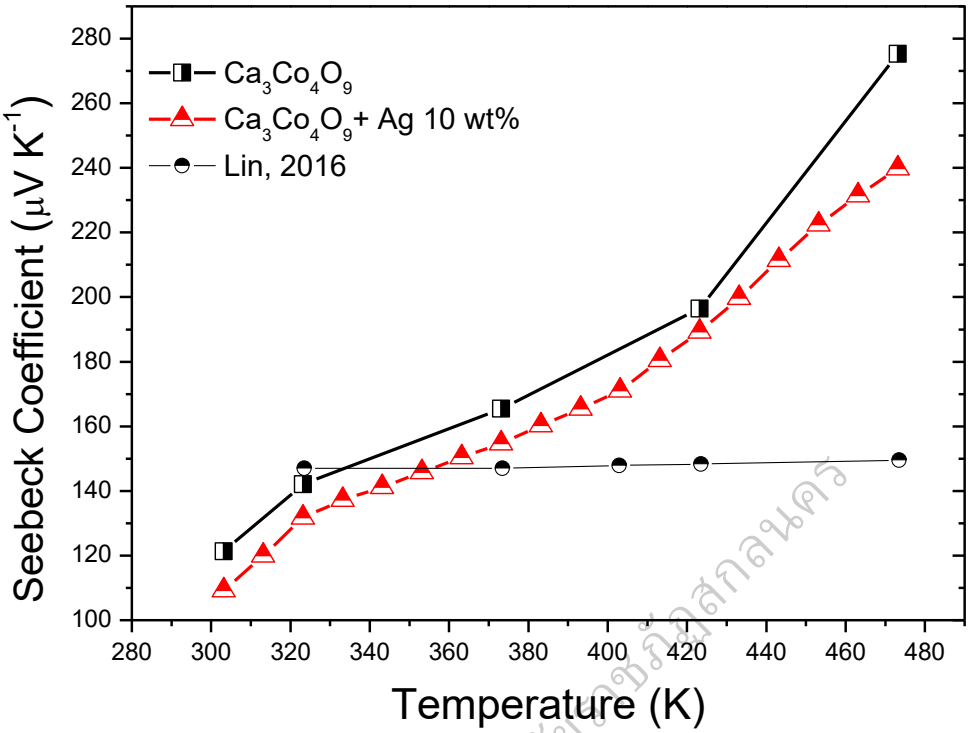

Figure 45 Temperature dependence of Seebeck coefficient for $Ca_3Co_4O_9$ + Ag 10 wt% and $Ca_3Co_4O_9$

The temperature dependence of the Seebeck coefficient (S) CCO + Ag sample similar to the pure CCO sample as shown Figure 45. The S of all the samples were increased with an increasing in temperature in positive type indicated to p-type materials. However, it obviously decreases with addition of Ag even with small amounts. This result expected to effect from Ag particle it was proposed that Ag particles play two roles in a thermoelectric samples: (1) the Ag particles dispersed in material act electrical connections between cobaltite grains, which has little influence on s ; and (2) the Ag particles agglomerated act as bypasses in carrier transports, which degrades S . This conclusion corresponds well to Yang et al. work on the relationship between S and Ag addition in CCO materials which in condition add Ag 10 wt% was decreased S slightly when compared with CCO un-doped (Wang, Sui, Wang, & Su, 2009). The S of CCO + Ag sample was decreased from CCO 12.89% at 473 K.

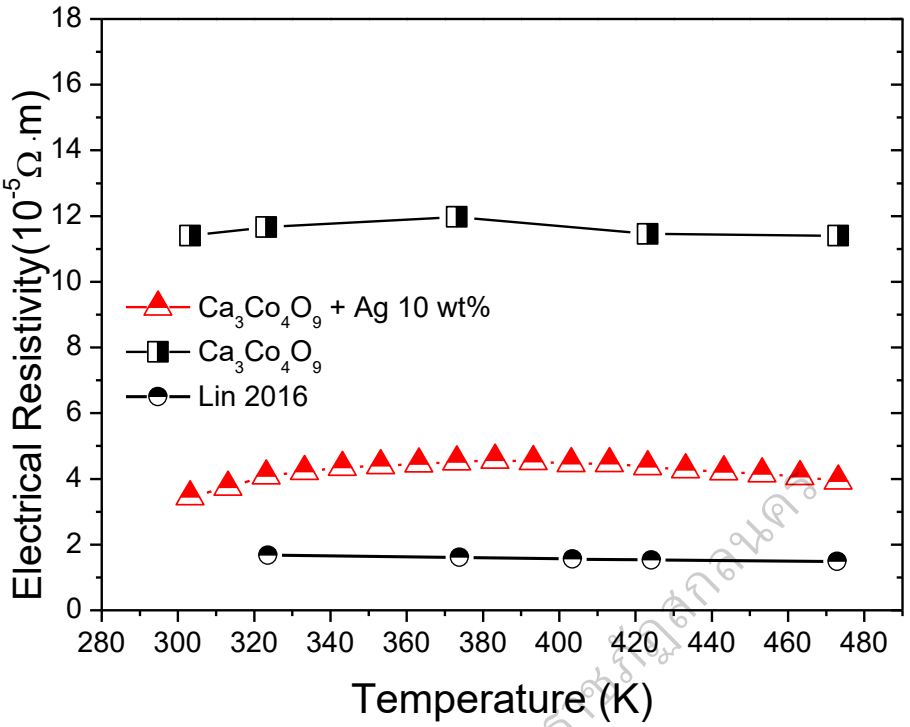

Figure 46 Temperature dependence of electrical resistivity for $Ca_3Co_4O_9$ + Ag 10 wt% and $Ca_3Co_4O_9$

The temperature dependence of resistivity (ρ) of CCO and CCO + Ag in the range from 303 to 473 K, is shown in Figure 46. All the samples show similar transport behavior, metallic–like behavior below about 380K and semiconducting–like behavior above about 380K. The resistivity decreases significantly with increasing Ag content, this phenomena was effected from dispersed Ag particle in material act to connections between cobaltite grains and increased mobility of the carrier scattering at the grain boundary will be reduced effectively or decreased activation energy. As previously reported, the misfit–layered CCO oxides have two–dimensional anisotropic electrical properties and the resistivity is mainly determined by the resistivity in the ab–plane (ρ_{ab}). The grain orientation enhances the domination of ρ_{ab}, that is, enhances the high orientation along (00l) plane in the sample. The carrier mobility for the CCO crystal along (00l) plane was higher than other directions. Therefore, the high orientation along (00l) plane promotes an increase in the electrical conductivity but with little influence on the Seebeck coefficient. The ρ of CCO + Ag sample was decreased from CCO 65.47% at 473 K.

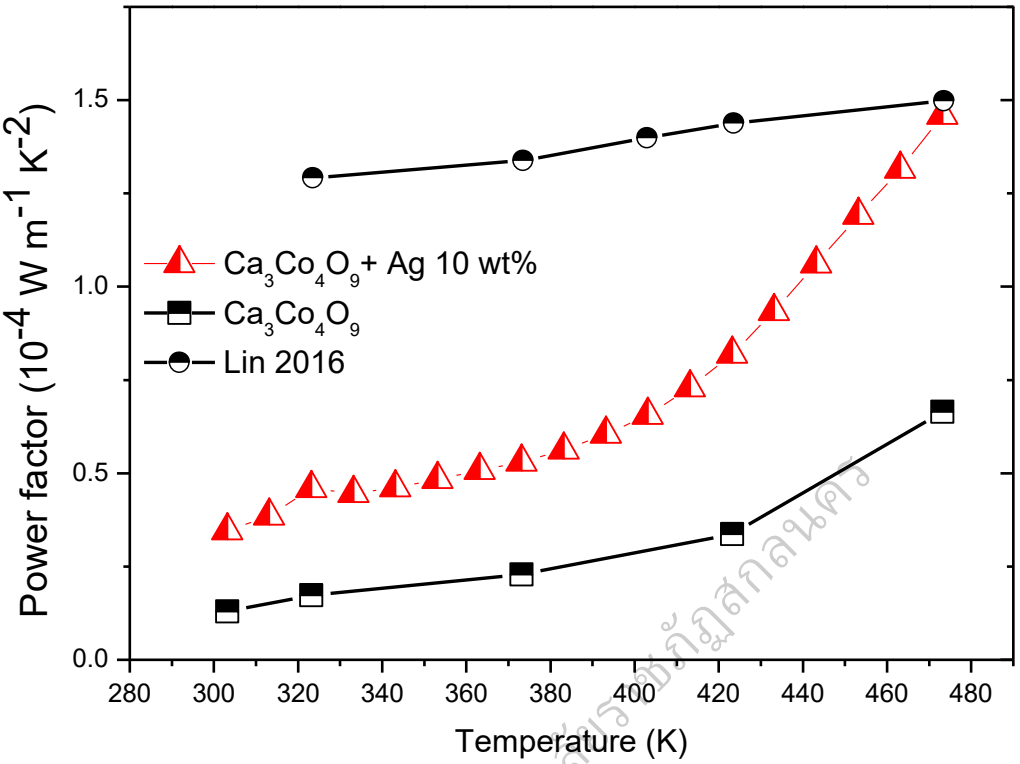

Figure 47 Temperature dependence of power factor for $Ca_3Co_4O_9$ + Ag 10 wt% and $Ca_3Co_4O_9$

The power factor (P) of CCO + Ag and CCO samples were calculated by using S and ρ values. The temperature dependence of P for these samples at 303 K to 473 K, is shown in Figure 47. It is seen that the P of all samples increase with an increase in temperature. Although the s decreases slightly with the addition of Ag but in ρ was decreased more CCO so the samples except for CCO+ Ag shown higher power factor than CCO. Then the P was increased and expected over the temperature range higher than 473 K.

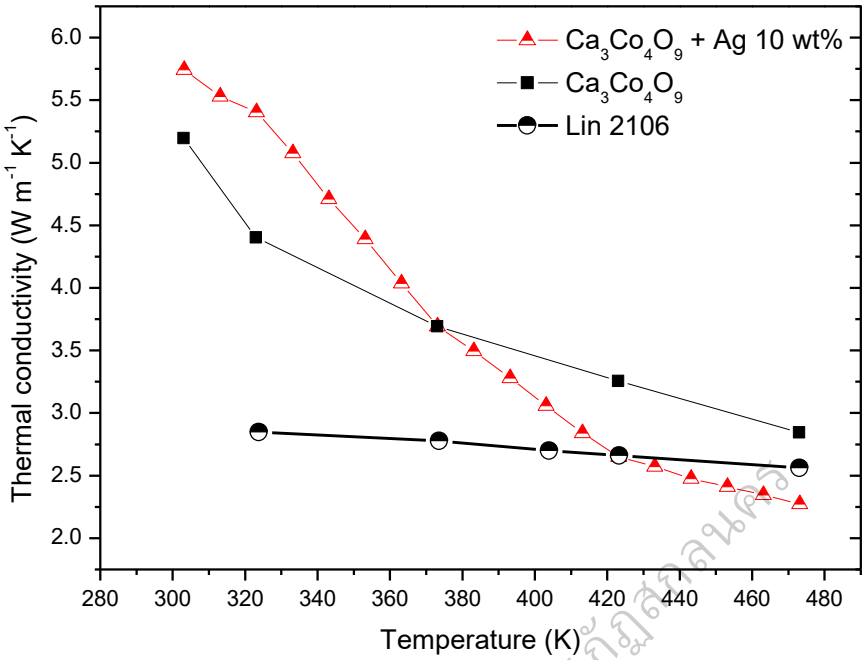

Figure 48 Temperature dependence of thermal conductivity for $Ca_3Co_4O_9$ + Ag 10 wt% and $Ca_3Co_4O_9$

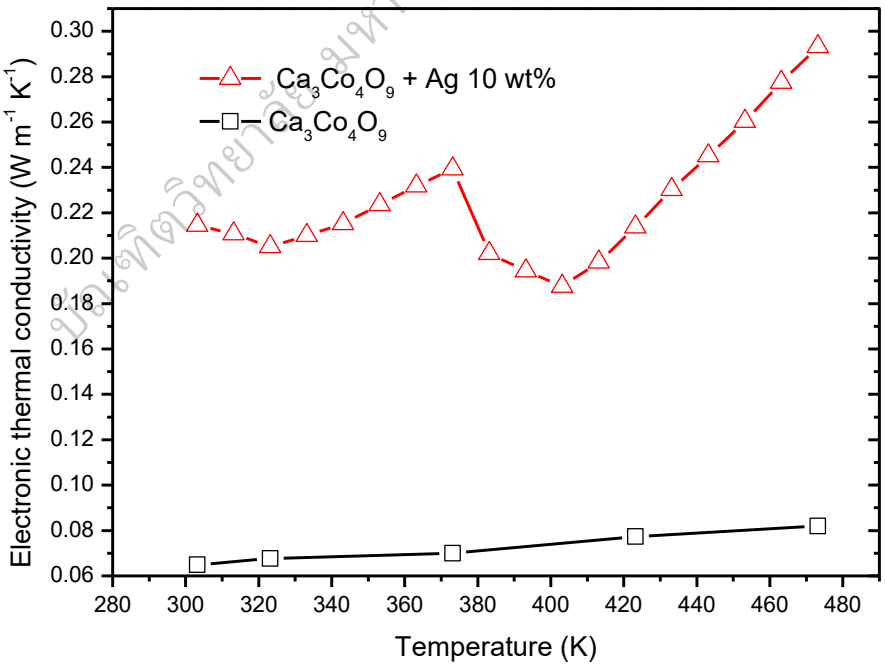

Figure 49 Temperature dependence of electronic thermal conductivity for $Ca_3Co_4O_9$+Ag 10 wt% and $Ca_3Co_4O_9$

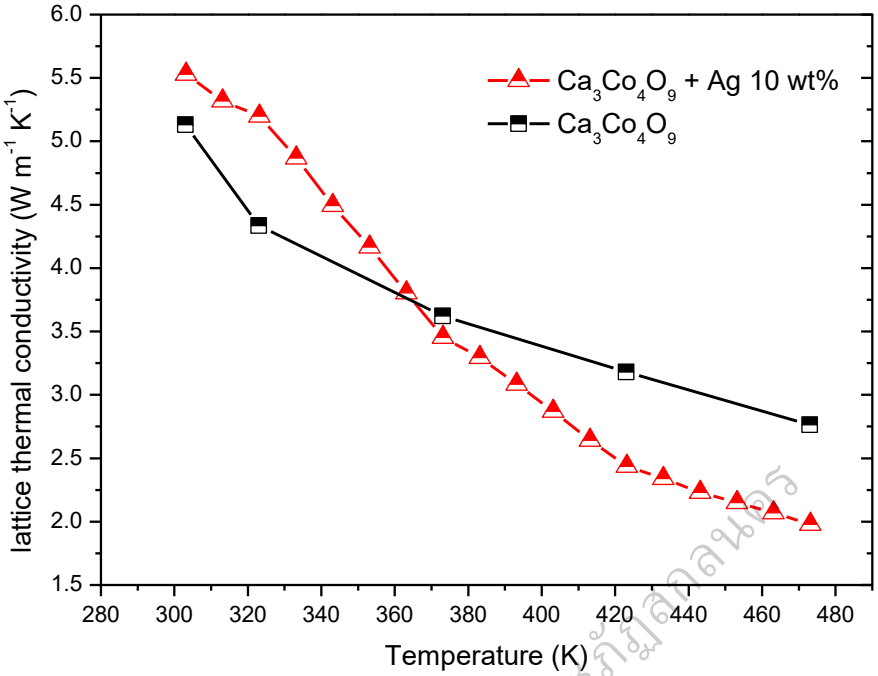

Figure 50 Temperature dependence of lattice thermal conductivity for $Ca_3Co_4O_9$ + Ag 10 wt% and $Ca_3Co_4O_9$

The temperature dependence of thermal conductivity (κ) for CCO + Ag and CCO at 303 K to 473 K as shown in Figure 48. The κ of all sample were decreased with increasing temperature. In addition, the κ in CCO + Ag sample exhibited high more than CCO due to effect of Ag dispersed between cobaltite grains not only reduces carrier scattering, but also contribute a good conductivity for phonon. When temperature above 373 K the κ of CCO + Ag sample decreased more than CCO this behavior expected from oxygen vacancy and porosity in sample which low more than CCO. The electronic thermal conductivity was calculated from Wiedemann–Franz's law equation by using electrical resistivity. The κ_e of CCO+ Ag was increased with increasing temperature because of ρ decreased shown in Figure 49. Then compared between κ, it was clearly the major of value got from the κ_l shown in Figure 50. So that, the reduction in lattice thermal conductivity could be related to the strong scattering of phonons caused by the increased grain boundaries and fine Ag particle or point defects resulting from the addition of Ag. The κ of CCO + Ag sample was decreased from CCO 20.11% at 473 K.

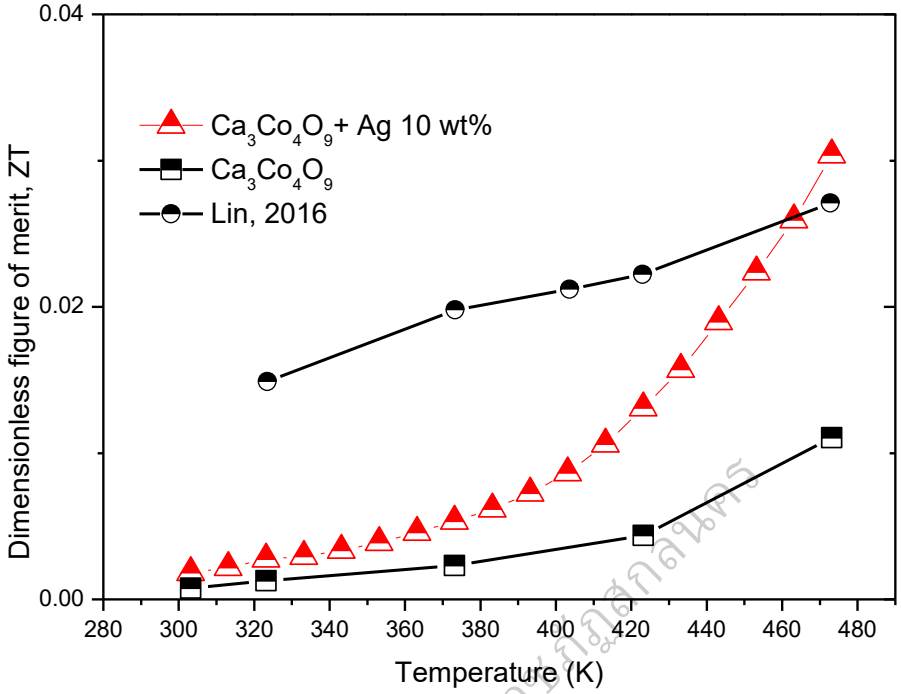

Figure 51 The temperature dependence of the dimensionless figure of merit (ZT)

The temperature dependence of the dimensionless figure of merit (ZT) for CCO + Ag and CCO as shown in Figure 51. The ZT value was calculated by using S , ρ , κ values and absolute temperature T of the sample . The ZT value of CCO + Ag can exceed 0.03 at 473 K, which higher than CCO 2 time (Lin, et al., 2016), and this ZT value is quite high for a ceramic material. These results suggest that this samples could be a good candidate for high temperature thermoelectric application. In addition, The Ag on sample was expected for connection between silver pastes on fabrication process which corresponding previous work (Funahashi, et al., 2006)

THERMOELECTRIC CELL

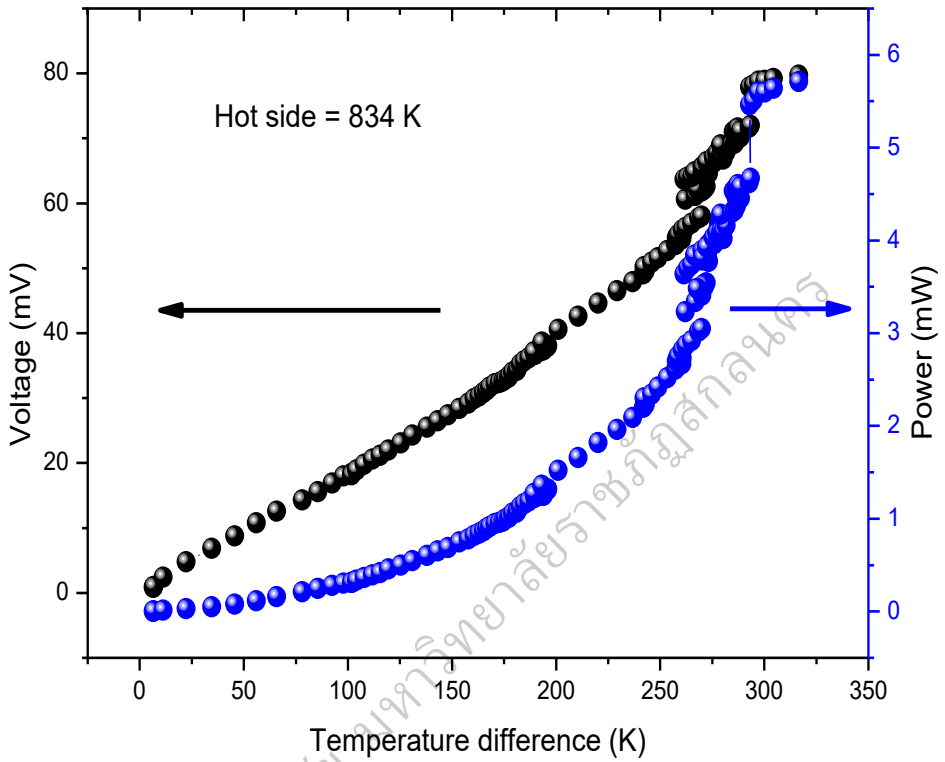

Figure 52 Relationship between voltages, electrical power and temperature difference of ∏–shape thermoelectric cell 2 pair at high temperature

Relationship between open circuit voltages, electrical power and temperature difference of ∏–shape thermoelectric cell 2 pair at 834 K, are shown in Figure 52. The heat source for high temperature was used butane gas burner in to TE cell and water cooling used for could side. The TE cell 2 pairs had been generating maximum electrical power and open circuit voltage 5.71 mW and 80 mV, respectively. Thermoelectric failure was limited by alumina substrate due to broken at 978 K. So that, the thermoelectric module uncover on top for decreased thermal resistant from alumina and apply to appropriate other substrate such as aluminum nitride, thin synthetic mica, boron nitride etc.

THERMOELECTRIC MODULE

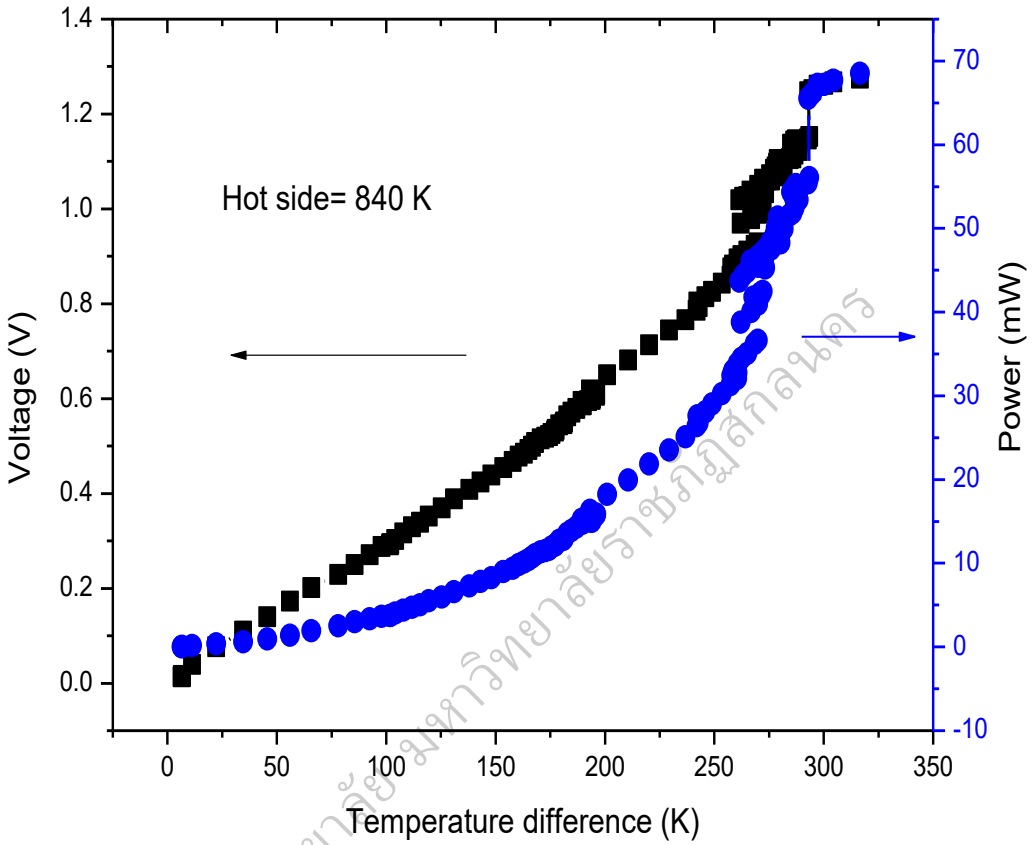

Figure 53 Relationship between voltages, electrical power and temperature difference of ∏–shape thermoelectric module at high temperature

The relationship between open circuit voltages, electrical power and temperature difference of thermoelectric module 32 pair at 840 K, are shown in Figure 53. The heat source for high temperature was used heater wire in to TE cell and water cooling used for could side. The TE module 32 pairs had been generating maximum electrical power, open circuit voltage and efficiency 68 mW, 1.27 V and ≈ 1.5 %, respectively.

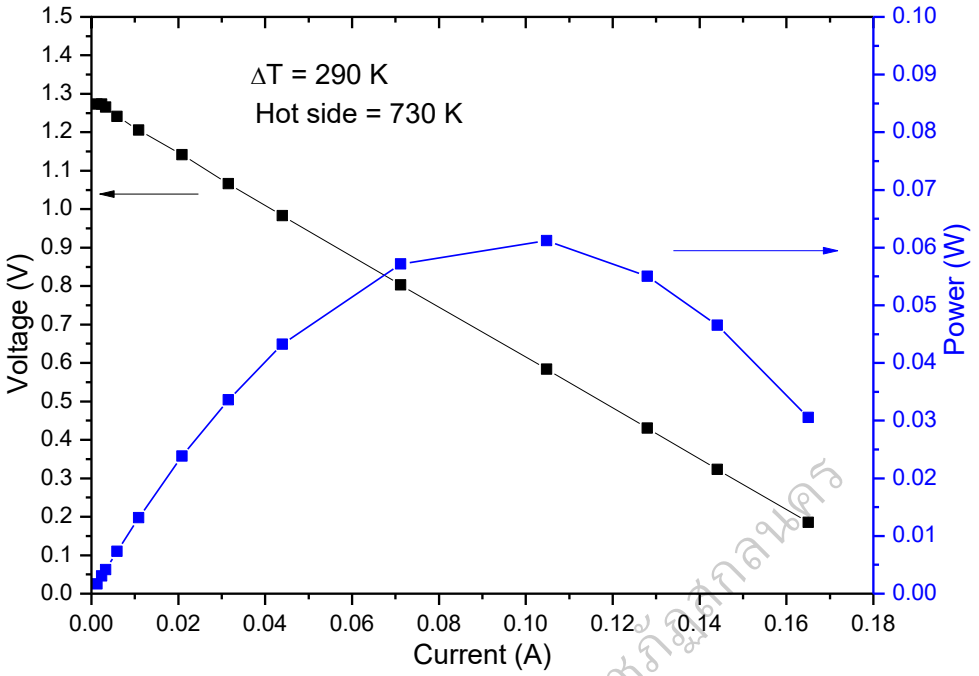

Figure 54 The *I–V* and *I–W* curves of 32 pair thermoelectric module as a function of temperature difference at T_h= 730 K

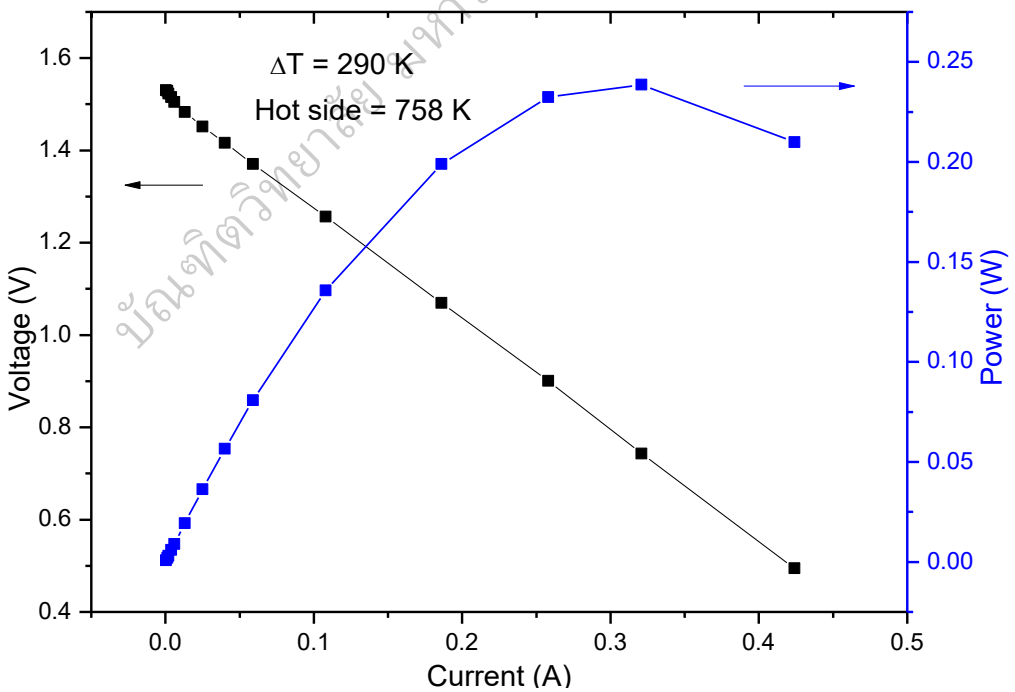

Figure 55 The *I–V* and *I–W* curves of 50 pairs thermoelectric module commercial as a function of temperature difference at T_h= 758 K

The *I–V* and *I–W* curves of 32 pairs thermoelectric module of n–$Ca_{0.97}Bi_{0.03}MnO_3$ and p–$Ca_3Co_4O_9$ +Ag 10 wt% under T_h=730 K and ΔT = 290 K, are shown in Figute 54. The measured open circuit voltage and maximum output power are 1.23 V and 66 mW, respectively. The matching load for TE module was nearly internal resistant of module so to decrease the internal resistant was important for improve performance of TE module. When compared our module with commercial oxide thermoelectric module 50 pairs a matching load was confirmed and power density per leg average 2.38 mW/leg and our TE module generated 1.03 mW/legs shown in Figure 56.

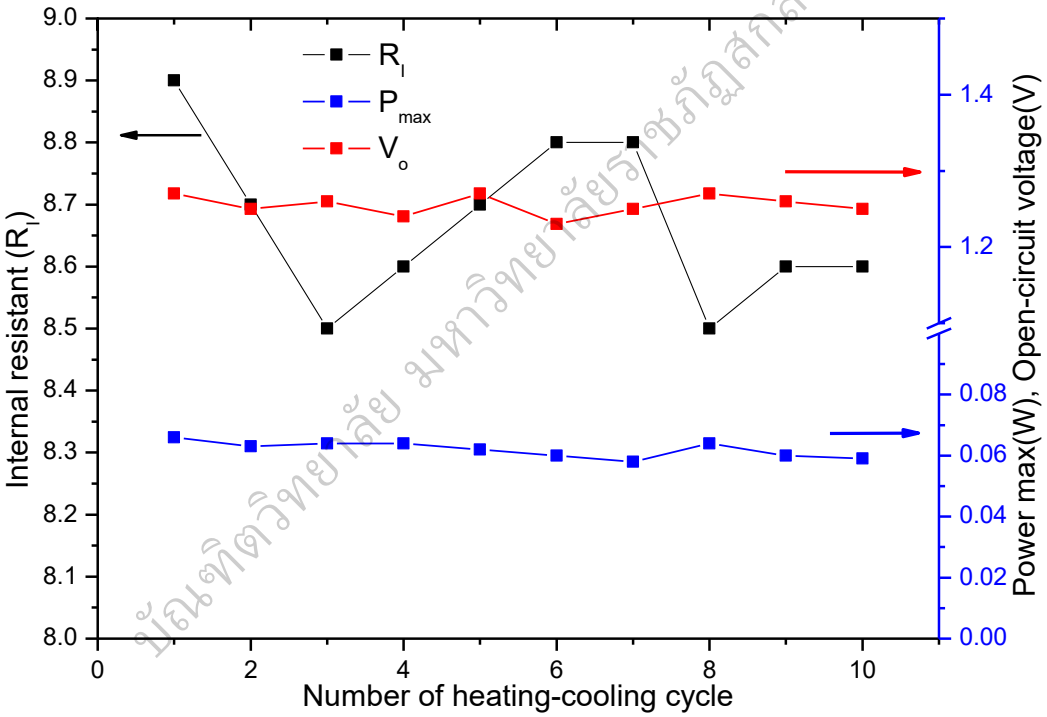

Figure 56 The stability of thermoelectric module at high temperature at 730 K

The TE module required a stability for long time working at high temperature so the internal resistant of TE module are important. relationship between internal resistant (R_I), power max (P_{max}), open circuit (V_o) and number of heating and cooling cycle, respectively as shown in Figure 56. The R_I of TE module before test is 8.7 Ω at room temperature then TE was tested in 10 cycle at hot side 730 K.

The R_l in all cycle non-significant change so stability were confirmed goodness joints all past in the module. The P_{max} and V_o shown stability for generation electricity in all cycle then the application in brick furnace was expected to stable and good working in long time.

THERMOGENERATOR APPLICATION

The thermogenertor installed to brick furnace heat source for generate electricity. Thermogenerator system consist of 5 module connected series on aluminum hot plate and a water cooling was placed over the module. Hot side for used with system around 583 K a thermogenertor generated maximum electricity about 27 W and average about 18 W for charging battery shown in Figure 57. Lighting system electric load 15 W used for brick furnace in Theerawut commerce were successfully and charged battery from 11.4 V to 12V 7.5 Ah in 3.5 h continues.

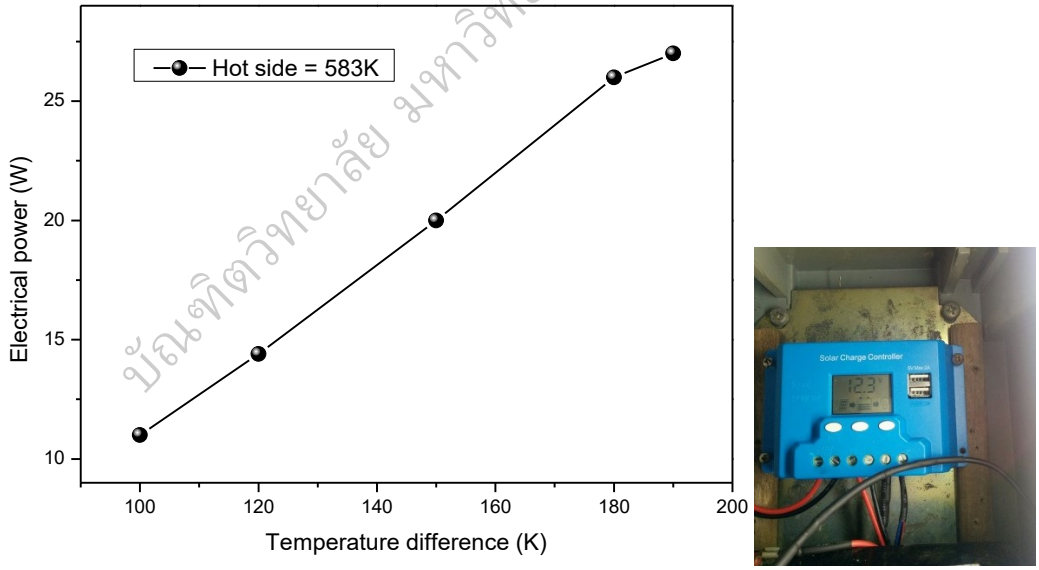

Figure 57 The relationship between electric power and temperature difference of Thermoenerator system and charging to battery